AIAA JOURNAL
Vol. 50, No. 9, September 2012

Unsteady Flow Analysis of a Multi-Element Airfoil Using Lattice Boltzmann Method

Rajani Satti,* Yanbing Li,† Richard Shock,‡ and Swen Noelting§
Exa Corporation, Burlington, Massachusetts 01803

DOI: 10.2514/1.J050906

High-lift devices employed on modern aircraft are significant contributors to overall airframe noise. In this paper, a lattice Boltzmann method with a very large eddy simulation approach is applied to computationally investigate the aerodynamic and aeroacoustic behavior of the flow around a generic high-lift configuration (three-element airfoil) at low Mach number. Three-dimensional time-dependent nearly incompressible simulations were conducted at different angles of attack to capture the instantaneous and mean flowfields around the airfoil, previously predicted by Navier–Stokes studies. The computed mean flow results showed good agreement with existing experimental and numerical data, which include the pressure distributions around the elemental surfaces and the time-averaged mean flowfield within the slat cove. As a major objective of the present study, the unsteady flow simulations were used to capture the slat cove unsteadiness, a source of both broadband and narrowband noise. In particular, the effect of angle of attack on the shear layer emanating from the slat cusp, slat trailing-edge vortex shedding, convection, and reattachment of vortical structures near the slat gap were explored by the present simulations. Consequently, the acoustic implications of such complex unsteady flow phenomenon within the slat cove were explained and discussed in detail.

Nomenclature

k	=	turbulent kinetic energy
S_{ij}	=	rate of strain tensor
T	=	temperature
U^+	=	U/u_τ, dimensionless velocity
u_τ	=	$\sqrt{\tau_w/\rho}$, friction velocity
y^+	=	yu_τ/ν_0, dimensionless distance
ε	=	turbulent dissipation
ν_0	=	kinematic viscosity
ρ	=	density
τ_{ij}	=	Reynolds stress tensor
τ_w	=	wall shear stress

I. Introduction

IN RECENT years, the study and mitigation of airframe noise [1,2] has gained significant interest among the aerospace community due to ever increasing regulations on aircraft noise around airports and technological advances in reducing engine noise. During approach conditions, high-lift devices such as leading-edge slats, trailing-edge flaps, blown flaps, vortex generators, etc. are major contributors to the overall airframe noise. Specifically, recent model scale tests [3–7] have characterized the leading-edge slat as a prominent source of acoustic noise. The complex unsteady fluid flow and associated acoustic phenomena around the leading-edge slat pose a challenging problem for both experimental and numerical studies. The present study is therefore focused on simulating the prominent unsteady flow features and related acoustic phenomenon around a typical high-lift setting using a novel, computational fluid dynamics (CFD) approach based on the lattice Boltzmann method.

Presented at the 46th AIAA Aerospace Sciences Meeting and Exhibit, Reno, NV, 7–10 January 2008; received 7 September 2010; revision received 9 December 2011; accepted for publication 11 December 2011.

*Senior Physics Validation Engineer. Senior Member AIAA.
†Manager, Physics Validation.
‡Director, Physics Validation and Support.
§Managing Director, Aerospace.

The test configuration employed in this study is a generic three-element airfoil (with a leading-edge slat) known in existing literature as the MDA30P30N model (Fig. 1). As detailed by Rumsey and Ying [8], the flowfield around such multi-element airfoils is generally characterized by complex flow phenomenon such as formation and convection of shear-layer vortices, flow separation and reattachment, laminar–turbulent flow transition, wake interactions, etc. More importantly, the flow unsteadiness around the leading-edge slat is of interest because it has its own subdomain of geometry-dependent unique flow characteristics such as the shear-layer evolution and breakup, flow recirculation and reattachment, and, above all, the classic trailing-edge vortex shedding. These complex flow features within the slat cove inevitably cause flow fluctuations that can escape to the far field as broadband noise (due to unsteady vortical structures within the slat cove [9–12]) as well as tonal noise (due to trailing-edge vortex shedding [13,14]).

Based on the previous discussion, it is imperative that the combination of geometric complexity and the acoustic phenomena associated with the leading-edge slat demands an in-depth analysis of the slat cove unsteadiness, thereby posing major challenges for both experiments and computational studies. Fortunately, advances in measurement techniques and instrumentation coupled with increased computing resources and state-of-the art turbulence modeling methods have led to significant progress in the design and analysis of high lift aerodynamic systems. From an experimental perspective based on nominally two-dimensional high-lift configurations, hot wire anemometry has been extensively used by many researchers [15–17] to survey the flowfield in the near-wake and near the slat trailing-edge region, measure shedding frequencies, and identify potential noise producing structures through the slat gap. In fact, a recent study by Rumsey et al. [18] used hot film sensors to measure laminar-to-turbulence transition locations on each element. This study is noteworthy because accurate measurement of transition location provides valuable information for numerical methods to improve the prediction of incoming boundary layer thickness, which has a direct impact on the slat unsteadiness predictions.

On a related note, nonintrusive flow diagnostic systems like laser Doppler velocimetry and particle image velocimetry have also been used recently to probe the flowfield in multi-element airfoil configurations [19,20]. More relevant to the present work is the PIV investigation of Jenkins et al. [21], who investigated the unsteady flow near the leading-edge slat of a two-dimensional generic multi-element airfoil configuration. Instantaneous velocities obtained from PIV images were used to obtain mean and fluctuating components of

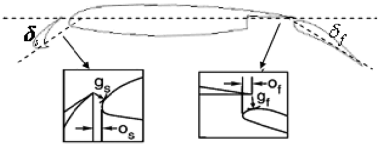

Slat angle, δ_s	30°
Flap angle, δ_f	30°
Slat Gap, g_s	2.95%
Flap Gap, g_f	1.27%
Slat Overhang, o_s	-2.5%
Flap Overhang, o_f	0.25%

Fig. 1 Schematic of the MDA30P30N model.

velocity and vorticity. Their measurements were used to examine the shear-layer formation near the slat cusp, vortex shedding at the slat trailing edge, and the convection of vortical structures through the slat gap, which revealed the complex unsteady flow phenomena inside the slat cove and around the slat trailing-edge region. Further, instantaneous snapshots of PIV images were used to depict the different states of the unsteady flow within the slat cove and the trailing-edge region.

Because experiments for such unsteady flow investigations are generally expensive and time consuming and can only provide limited data due to lack of convenient and nonintrusive access, CFD methods [Reynolds-averaged Navier–Stokes (RANS), large-eddy simulation (LES), and detached-eddy simulation] have been extensively used for both aerodynamics and aeroacoustics analysis in the past 10–15 years [22–24]. Generally, time-accurate unsteady RANS (URANS) simulations are regarded as one of the most common CFD methods used to provide the unsteady flowfield information around realistic airframe noise components. In this context, the work done by Khorrami et al. [9,13,25] as well as Choudhari and Khorrami [26,27] is remarkable, owing to their contribution in exploring the applicability of CFD to understand the complex unsteady physics around the slat cove region. The early work of Khorrami et al. [9,13] modeled a fully turbulent flowfield around the slat region and provided insight into the dominant noise source mechanisms around a high-lift configuration. However, their computations were found to be overly diffusive and thus prevented the development of cove flow unsteadiness. In a second study, Khorrami et al. [10] and Choudhari et al. [11] applied a simple zonal approach, whereby the turbulence production term was completely turned off in the slat cove region to capture the flow unsteadiness. Based on this approach, Khorrami et al. [25] recently conducted 2D simulations of a generic three-element airfoil (MDA 30P30N model), whereby good agreement was obtained for mean flow properties. However, their 2D simulations showed that the predicted shear-layer vortices and recirculation zone were more energetic in comparison with experiments [21], thereby leading to significant discrepancies in predicting unsteady vortical structures. In an attempt to resolve this discrepancy, they later extended their work to a 3D URANS study [26,27] to evaluate the 3D effects on the flow structures within the slat cove region and their implications for the far-field noise. The 3D simulations were used to investigate the local and global dynamics of large-scale, three-dimensional vortical structures. The analysis showed relatively high local turbulence intensity and peak surface pressure fluctuations near the reattachment region along the lower slat surface. It was inferred that the reattachment region played a key role in the generation of slat broadband noise. Unlike the previous 2D studies, external forcing near the slat cusp to accelerate the development of 3D vorticity structures was applied only for a short duration of time. Further, the computed acoustic characteristics resembled the previously reported, subscale measurements of slat noise [28].

Apart from the traditional CFD solvers, recent advances in the kinetic-theory-based lattice Boltzmann method (LBM) have made it a promising alternative CFD approach for complex flow simulations [29]. LBM describes fluid flow in terms of a discrete kinetic equation for particle density distribution functions, the lattice Boltzmann equation (LBE). The macroscopic flow properties such as density, momentum, and energy are direct results of the moments of these particle distribution functions, and the pressure can be obtained through an equation of state rather than solving a Poisson equation in the incompressible Navier–Stokes (NS) equation [29]. The commonly used LBM scheme applies a second-order approximation of the continuum Boltzmann kinetic equation and has been shown to recover the compressible NS equation at small Mach numbers (the nearly incompressible limit) [30,31]. A number of numerical benchmarks have been presented to illustrate the accuracy of LBM for doing direct numerical simulations of low-Reynolds-number flows at nearly incompressible flow regime [29,32,33].

It should also be noted that, although LBM cannot entirely recover the incompressible Navier–Stokes equations, there are several notable works in the literature where models were proposed to develop a lattice Boltzmann approach for representing the incompressible Navier–Stokes equation appropriately. For example, He and Luo [34] maintained a constant density with LBM, wherein pressure, instead of the mass density, was treated as an independent dynamic variable, and compressible effects were eliminated by neglecting the second-order dependence on Mach number. Chen et al. [35] solved the lattice Boltzmann scheme of vorticity stream function to model incompressible axisymmetric flows. Also, Fu and So [36] proposed to expand the particle equilibrium distribution function with a second-order polynomial in velocity space to represent incompressible flows so that the constant density NS equation can be recovered exactly from the modeled LBE.

Turbulence modeling has been incorporated into the LBM approach and has been demonstrated as a viable and desirable approach for doing very large eddy simulations (VLESs) of high-Reynolds-number turbulent flows [32,37]. This approach accurately and robustly predicts time-dependent aerodynamic behavior of turbulent flow, including the effects of complex detailed geometry. Over the past 10 years, the LBM–VLES approach has been successfully implemented in the automotive segment to accurately compute unsteady flows and capture aeroacoustic phenomenon including buffeting, wind noise, and wall pressure fluctuations [38,39]. Because of its inherent transient and compressible nature, the LBM-based approach allows for bidirectional coupling between the aerodynamic excitation and acoustic response. Beyond the automotive sector, we recently started exploring the application of the LBM–VLES approach for aerospace applications (both aerodynamics and aeroacoustics) involving high-lift systems [40–43] and landing gears [44]. Preliminary simulations for the aforementioned configurations readily captured the mean flow properties as well as the complex unsteady flow phenomenon.

In the present study, an LBM–VLES method is applied for the study of flowfield around a generic three-element airfoil configuration presented by Jenkins et al. [21] and Khorrami et al. [25]. Two obvious questions provided the motivation for the present study:

1) Can the LBM approach predict the fluid flow characteristics in a complex geometry (like the slat element) on par with traditional URANS solvers?

2) Will the time-accurate LBM approach capture the complex unsteady flow physics and associated acoustic implications in the slat region?

The simulations and the subsequent results presented in this paper provide a positive answer to both of these questions. Similar to the work of Choudhari and Khorrami [27], 3D time-dependent simulations were conducted to capture the global and local flow structure details over a three-element airfoil. This paper is organized as follows. First, a description of the studied problem is given (Sec. II). Next, the details of the LBM–VLES algorithms are provided (Sec. III). This is followed by the generated results (Sec. IV) and the conclusions (Sec. V).

II. Problem Description

The three-element configuration used in this study is a McDonnell–Douglas (currently Boeing) airfoil known as the MDA30P30N model (Fig. 1) in existing literature. It consists of three

components: the slat, the main, and the flap elements. The important geometric settings, which are the gaps and the overhangs, are provided in Fig. 1. More information related to the geometry is discussed in detail by Jenkins et al. [21]. The simulation conditions are the same as the one used in the experiments conducted in the Basic Aerodynamic Research Tunnel (BART) at NASA Langley Research Center. The fluid under consideration is air with an inflow velocity of 56 m/s at the inlet, which corresponds to a freestream Mach number of 0.17 and a Reynolds number of 1.7 million based on the stowed chord length. The inflow boundary is specified at 1.5 m away from the leading edge of the airfoil, and the outflow boundary is located at 6.0 m downstream from the trailing edge of the airfoil, with a constant static pressure outflow condition being imposed. The top and the bottom walls of the wind tunnel are included with the same height of 0.711 m as in the BART tunnel. It should also be noted that both no-slip and free-slip boundary conditions were tested on the tunnel walls. Because there was no significant effect on the flow characteristics, for computational simplicity, the final computations were conducted using the free-slip boundary conditions at the tunnel walls. For the 3D simulation, the 2D airfoil profile is extruded in the spanwise direction with a width around 6.67% of the stowed chord. Several preliminary studies with different spanwise extents varying from around 3% to 12% were conducted to ensure that the unsteady, three-dimensional effects were well captured with a smaller spanwise width to minimize computational cost.

For the boundary condition on the airfoil surface, the existing literature indicates that a significant portion of the airfoil surface will be within laminar and laminar-turbulence transition region. Modeling this region as fully turbulent in simulation will introduce excessive friction forces to the near-wall fluid, resulting in a relatively low fluid velocity in the near-wall region. Such low fluid velocities can strongly affect the surface pressure distributions as well as the flow separation behavior. Because the current LBM–VLES approach does not incorporate predictions for natural transition from laminar to turbulent flow, the following approach is adopted to approximate the reduced surface skin friction force effect in such flow regions. First, transition locations extracted from experiment (Rumsey et al. [18], based on hot film measurements) at an angle of attack of 8 degree were used to identify the laminar and turbulent regions on the elemental surfaces. The wall skin friction was then turned off from airfoil leading edge up to the transition point. Fully turbulent wall boundary conditions were applied for the remaining surface portions. For other angles of attack (4 and 6), because no transition location data was available, similar boundary condition treatment as for AOA = 8 case was applied. It should be noted that the flow and tunnel conditions in the study of Rumsey et al. were different from the current one. A Mach number of 0.2 and Reynolds number of 9 million were used in the study of Rumsey et al. It should be noted that the aforementioned strategy is essentially applying free-slip wall boundary condition on the laminar/laminar-turbulence transition regions. This strategy proved to be reliable, as seen in the surface pressure plots presented in later sections.

In this study, a Cartesian grid system with cubic cells is used for the flowfield, for important flow regions (such as slat cusp, slat trailing edge, and flap trailing edge) where strong velocity gradients are expected, local refinements are applied. This is achieved by applying variable resolution (VR) regions in the simulation domain. A typical VR setup for this study is shown in Fig. 2; the details of the grid system near the slat element and flap element is also shown here. As can be observed, the finest resolution of 0.074 mm per cell size was applied in the slat trailing-edge region; this allows approximately five cells to resolve the slat trailing-edge region (which has a finite thickness of 0.36 mm). Each bounding box represents one grid resolution level, and VRs cascade outward from the fine-resolution region toward the coarse-resolution region. It should be noted here that the flow regions near the slat shear layer, slat main element gap region, and main flap element gap region have the second-level grid refinement for capturing the flow unsteadiness generated. Besides that, the flow region near element boundaries are generally covered by a VR level with resolution of 0.297 mm per cell size, which gives an average y^+ value in the range of [50:200]. Resolutions differ by a factor of 2 between two adjacent VR regions. A detailed discussion on the VR algorithm can be found in [45]. A surface grid representing solid geometry is overlaid on the Cartesian mesh to generate the fluid/solid interface. The particle density distribution functions are cell-centered, and the particle interacts with its neighborhood, either fluid particle or solid boundary to generate fluid dynamics. For a solid boundary that is not lattice cell-aligned, partial cells are generated, and a fraction of the particles (based on geometrical cell fraction) are used for the fluid/fluid and fluid/solid dynamics [32,46]. The particle–solid interaction (implementation of boundary condition) is straightforward in the LBM calculations; it ensures the conservation of local mass and momentum and enables the exact treatment of solid boundaries [46]. This strategy greatly reduces the time needed to generate boundary-conforming grids for complicated geometries. In the current study, a total number of 21 million fluid cells and 2.34 million surface elements are used. The simulation for one angle of attack was run approximately 1 million time steps to achieve final convergence; this corresponds to 0.138 s in physics time (with 1.3e − 7 s per time step), which is roughly 17 flow pass times

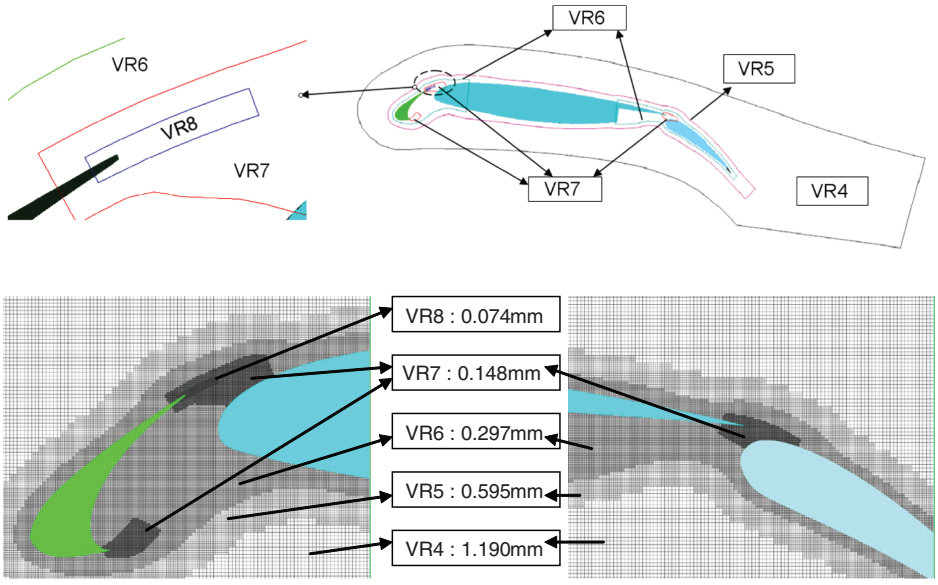

Fig. 2 Schematic view of VR regions applied in the current study (top right) with local zoom-in of the slat trailing-edge region (top left) and the details of the grid distribution in the vicinity of the slat (bottom left) and the flap (bottom right) elements.

(defined by incoming flow velocity and main element chord length). In terms of performance, the simulation takes about 150 h on a 122-core Linux cluster.

III. Numerical Algorithm

A. Lattice Boltzmann Method

The lattice Boltzmann equation has the following form:

$$f_i(\mathbf{x} + \mathbf{c}_i\Delta t, t + \Delta t) - f_i(\mathbf{x}, t) = C_i(\mathbf{x}, t) \tag{1}$$

where f_i is the particle distribution function moving in the ith direction, according to a finite set of the discrete velocity vectors $\{\mathbf{c}_i: i = 0, \ldots b\}$; $\mathbf{c}_i\Delta t$ and Δt are space and time increments, respectively. For convenience, we choose the convention $\Delta t = 1$ in the subsequent discussions. The collision term on the right-hand side of Eq. (1) adopts the simplest and also the most popular form known as the Bhatnagar–Gross–Krook form [30,31,47]:

$$C_i(\mathbf{x}, t) = -\frac{1}{\tau}[f_i(\mathbf{x}, t) - f_i^{\text{eq}}(\mathbf{x}, t)] \tag{2}$$

Here, τ is the single relaxation time parameter, and f_i^{eq} is the local equilibrium distribution function, which depends on local hydrodynamic properties. The basic hydrodynamic quantities, such as fluid density ρ and velocity $\mathbf{u}$, are obtained through moment summations:

$$\rho(\mathbf{x}, t) = \sum_i f_i(\mathbf{x}, t), \qquad \rho\mathbf{u}(\mathbf{x}, t) = \sum_i \mathbf{c}_i f_i(\mathbf{x}, t) \tag{3}$$

The three-dimensional D3Q19 model [31], shown in [41], is used in the present three-dimensional study to represent the possible velocity directions. The local equilibrium distribution function f_i^{eq} takes the following form so that the recovered macroscopic hydrodynamics satisfy the conservation laws and the leading order resulting macroscopic equations are Galilean invariant at low Mach number:

$$f_i^{\text{eq}} = \rho w_i\left[1 + \frac{\mathbf{c}_i \cdot \mathbf{u}}{T} + \frac{(\mathbf{c}_i \cdot \mathbf{u})^2}{2T^2} - \frac{\mathbf{u}^2}{2T} + \frac{(\mathbf{c}_i \cdot \mathbf{u})^3}{6T^3} - \frac{\mathbf{c}_i \cdot \mathbf{u}}{2T^2}\mathbf{u}^2\right] \tag{4}$$

where w_i are weighting parameters:

$$w_i = \begin{cases} 1/18, & \text{in 6 coordinate directions;} \\ 1/36, & \text{in 12 bi-diagonal directions;} \\ 1/3, & \text{rest particles} \end{cases} \tag{5}$$

and T is the lattice temperature, which is generally set to $1/3$ for isothermal simulations. In the low-frequency and long-wavelength limit, one can recover the Navier–Stokes equations through Chapman–Enskog expansion. The resulting equation of state obeys the thermally perfect gas law, $p = \rho T$. The kinematic viscosity of the fluid is related to the relaxation time parameter τ by [29–31]:

$$\nu_0 = (\tau - 1/2)T \tag{6}$$

When τ is close to 0.5, fluid viscosity is small, and particle distributions may become negative under certain extreme situations and numerical instability can subsequently occur. To avoid such a situation, numerical protections to ensure positive state distribution are applied in the current LBM algorithm. This scheme takes the same form as the one published in [32]. It should also be noted that the current D3Q19 model is a second-order discretization scheme of the continuum Boltzmann kinetic equation [48]; thus is not applicable for flows in the high Mach number regime where deviations from local thermodynamic equilibrium can be significant. In the current study, because the Mach number for most of the interested flow region is low, the D3Q19 model is well suited.

The combination of Eqs. (1–6) forms our LBM scheme (LBM momentum solver) for fluid dynamics.

B. Fluid Turbulence Model

To model the turbulent fluctuations, the LBE is extended by replacing its molecular relaxation time scale with an effective turbulent relaxation time scale; i.e., $\tau \to \tau_{\text{eff}}$, where τ_{eff} can be derived from a systematic renormalization group (RG) procedure [49] as

$$\tau_{\text{eff}} = \tau + C_\mu \frac{k^2/\varepsilon}{T(1 + \tilde{\eta}^2)^{1/2}} \tag{7}$$

where $\tilde{\eta}$ is a combination of a local strain parameter ($\eta = k|S|/\varepsilon$), local vorticity parameter ($\eta_\omega = k|\Omega|/\varepsilon$), and local helicity parameters. A modified k–ε two-equation model based on the original RG formulation describes the subgrid turbulence contributions [49,50] and is given by

$$\begin{aligned} \rho\frac{\mathrm{D}k}{\mathrm{D}t} &= \frac{\partial}{\partial x_j}\left[\left(\frac{\rho\nu_0}{\sigma_{k_0}} + \frac{\rho\nu_T}{\sigma_{k_T}}\right)\frac{\partial k}{\partial x_j}\right] + \tau_{ij}S_{ij} - \rho\varepsilon \\ \rho\frac{\mathrm{D}\varepsilon}{\mathrm{D}t} &= \frac{\partial}{\partial x_j}\left[\left(\frac{\rho\nu_0}{\sigma_{\epsilon_0\varepsilon}} + \frac{\rho\nu_T}{\sigma_{\varepsilon_T}}\right)\frac{\partial k}{\partial x_j}\right] + C_{\varepsilon_1}\frac{\varepsilon}{k}\tau_{ij}S_{ij} \\ &\quad - \left[C_{\varepsilon_2} + C_\mu\frac{\tilde{\eta}^3(1 - \tilde{\eta}/\eta_0)}{1 + \beta\tilde{\eta}^3}\right]\rho\frac{\varepsilon^2}{k} \end{aligned} \tag{8}$$

The parameter $\nu_T = C_\mu k^2/\varepsilon$ is the eddy viscosity in the RG formulation. All dimensionless coefficients are the same as in the original models [48,50]. The previous equations are solved on the same lattice using a modified Lax–Wendroff-like explicit time marching finite-difference scheme [51]. This LBE–VLES-based description of turbulent fluctuation carries flow history and upstream information and contains high-order terms to account for the nonlinearity of the Reynolds stress [49,52]. This is contrasted with its Navier–Stokes counterpart, which uses the conventional linear eddy viscosity-based Reynolds stress-closure models.

In the near-wall region, to avoid the high computational cost associated with fully resolving the turbulence boundary layer, a turbulent wall shear stress model is used to provide approximate boundary conditions for the near-wall cells [46,51]. It was coupled with a generalized LBM volumetric slip algorithm to realize the desired surface dynamics and ensure exact local mass and momentum conservations [46,53].

IV. Results and Discussion

As discussed in the previous sections, time-accurate LBM–VLES computations were performed for the three-element (MDA30P30N) airfoil at three different angles of attack of 4, 6, and 8 deg, respectively. Most of our discussion, however, would be limited to an angle of attack of 4 deg. In the following section, we first present the mean flowfield results around the three-element airfoil. Next, the unsteady flow predictions within the slat cove are analyzed and compared to experimental observations of Jenkins et al. [21]. Finally, the acoustic implications of the complex unsteady flow are explored and discussed in detail.

A. Mean Flow Structure

1. *Time-Averaged Surface Pressure Predictions*

The unsteady 3D simulation results were long-time-averaged to generate the mean flow results. As a first step, the mean pressure distribution around each element is compared with existing experimental (PIV) and numerical (2D URANS) data of Jenkins et al. [21] and Khorrami et al. [25]. Figure 3 shows the distribution of the pressure coefficient C_p, on the slat, main, and flap elements at two different angles of attack (AOAs) of 4 and 8 deg. Results show good agreement of LBM–VLES computations with that of existing CFD and experimental data.

For AOA of 4 deg, one can clearly observe that the mean pressure coefficient C_p of the most critical element (slat) is captured well by the present simulations. A remarkable difference between measured values and computed results is the overprediction of suction C_p of the

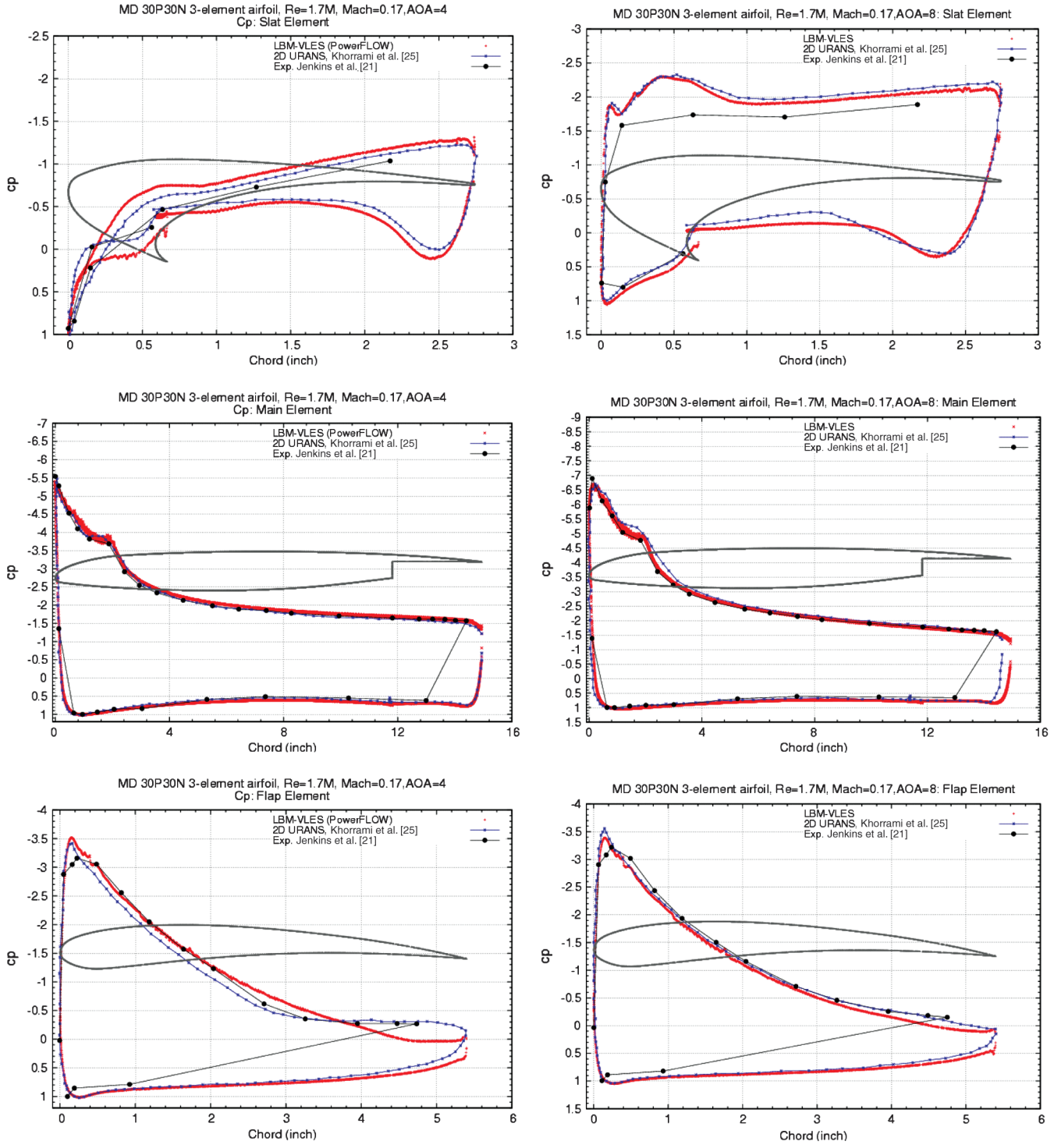

Fig. 3 Mean pressure distribution around different elements of the airfoil (CFD data from Khorrami et al. [25], PIV data from Jenkins et al. [21]).

aft of the leading edge along the slat top surface. This minor discrepancy in computed/measured results could be due to the specified transition location for this particular angle of attack. As mentioned earlier, the same transition location of AOA = 8 deg was also used for AOA = 4 deg due to the lack of experimental transition data from Rumsey et al. [18] for this angle of attack. The accurate prediction of the peak suction pressure on the main element illustrates the capability of the present LBM–VLES model in accurately predicting the slat gap region. On the flap element, the current study overpredicts the suction pick compared to the measured data, where, for other part of the leading-edge region on suction surface, the predicted pressure distribution agrees well with experiment data. However, the separation region along the flap trailing edge is not well predicted whereby computed results show only 20% separation compared to measured 40% separation of the flap chord. This discrepancy is in part attributed to possible inaccuracy in specifying the exact transition locations for this particular AOA. Other factors like trailing-edge resolution and limitation of the turbulence model in resolving pressure-driven flow separation may also contribute to the aforementioned discrepancy. At higher AOA of 8 deg, the LBM method again provided reliable predictions of the surface pressure distributions. Note that, at AOA of 8 deg, the flap surface pressure shows a fully attached flow, which is well predicted by the LBM method. Overall, except in the flap trailing-edge region, the LBM–VLES predictions were found to be on par with 2D URANS results.

2. Time-Averaged Slat Cove Flowfield

The main objective of the present study was to provide a better insight into the complex flow physics governing the slat cove region. In the following discussion, we present a detailed analysis of the mean flowfield including streamwise and vertical velocities, vorticity, and turbulent kinetic energy (TKE). Figure 4 shows the different mean flow contours at AOA of 4 deg. The LBM–VLES computations are compared to 2D URANS [25] simulations and measured data [21]. Observations of the streamwise and vertical velocity contours reveal important trends like flow acceleration near the slat cusp, weakening of flow acceleration near the slat cusp with increasing AOA, slat gap flow acceleration, and negative flow velocities near the wall being qualitatively well predicted by the present simulations. In contrast, similar to 2D URANS results, the LBM–VLES approach also shows higher negative cove velocities and higher slat cusp flow acceleration when compared to experimental results. Nevertheless, the most important flow feature near the slat cusp is the penetration velocity (i.e., penetration of flow) toward the cove wall. The present simulations accurately capture these penetration velocities, unlike the 2D URANS computations whereby the penetration velocity is overpredicted. As seen from Fig. 4, the normalized experimental streamwise velocity is around 0.227 in the slat cusp region. The LBM–VLES approach shows similar values around this region, whereas 2D URANS predicts a much higher value of 0.613.

Figure 4 also shows the averaged vorticity field comparisons between 2D URANS [25], experimental [21], 3D URANS [26], and LBM–VLES data for AOA of 4 deg. As evident from Fig. 4, the LBM–VLES-computed vorticity field shows excellent comparison to that of 3D URANS computations and experimental data. In particular, the LBM–VLES computations depict one-to-one comparison of the classic formation and propagation of a well-defined shear layer confined to a narrow spatial band to that of 3D URANS data. As for the 2D URANS results, the vorticity field was

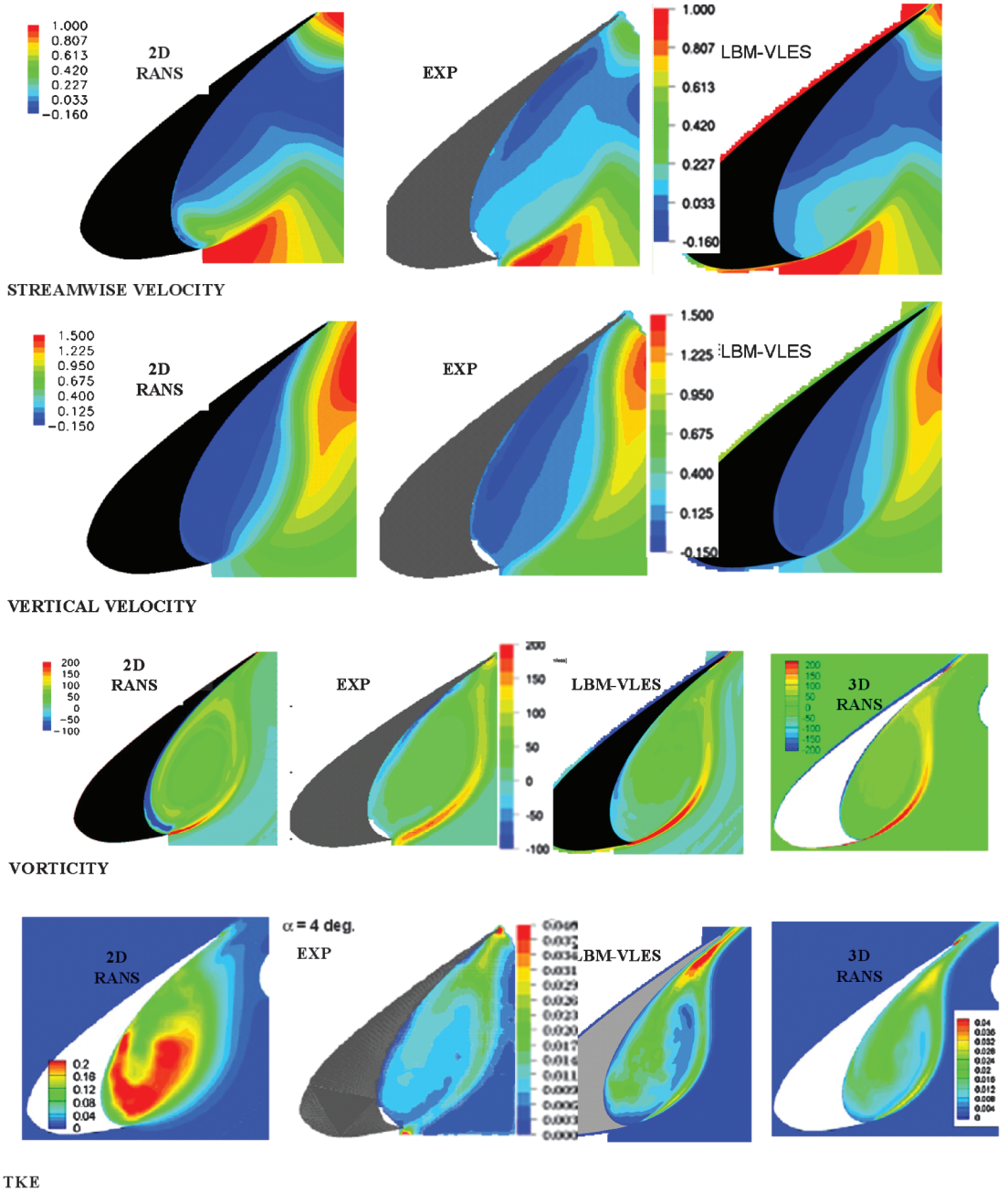

Fig. 4 Averaged streamwise and vertical velocity, vorticity, and TKE field at AOA = 4 (2D CFD images from Khorrami et al. [25], 3D CFD images from Choudhari et al. [26], experimental images from Jenkins et al. [21]).

found to be more diffused leading to unrealistic secondary and tertiary separations near the slat cusp. More information regarding the shortcomings of the 2D URANS results is provided by Khorrami et al. [25]. In contrast to the computations, a relatively thicker shear layer close to the cusp is obvious from experimental data [21]. This discrepancy, as stated by Choudhari and Khorrami [26], is attributed to the insufficient spatial resolution of the processed experimental data from PIV measurements [21], especially in the slat cusp region, whereby the large velocity gradients associated with a thin mixing layer are not adequately resolved.

It is well known that the statistics of turbulence (i.e., TKE) are closely related to the noise source [24,54]. Figure 4 also shows contours of computed and measured distributions of 2D TKE field. The LBM–VLES computations show a good qualitative comparison of TKE levels with experiments as well as 3D URANS results. Peak turbulent kinetic energy regions are confined mostly to the reattachment region, which was already identified as an active noise source within the slat cove (by Choudhari and Khorrami [27]). Higher TKE levels are also evident in the downstream locations of the slat cusp region. These predictions are consistent with the experiments of Jenkins et al. [21] and numerical simulations of Choudhari and Khorrami [27] as well as Imamura et al. [24].

Similar velocity, vorticity, and TKE comparisons were also obtained for other angles of attack of 6 and 8 deg and are not explained here. To summarize, the preceding results build confidence in using the LBM–VLES approach for mean flow as well as the turbulent statistics predictions in a generic high-lift configuration. As part of our present validation efforts, we next discuss our observation of some of the prominent unsteady flow features inside the slat cove region.

B. Instantaneous Flow Structure

Most CFD codes relating to simulations around a three-element airfoil have primarily focused on the mean flow characteristics. However, given the correlation between the noise sources and the instantaneous flow structures, it is crucial for any CFD code to obtain accurate predictions of local and global unsteady flow structures. In the following section, we investigate the instantaneous flow structures within the slat cove and compare the present simulations with the measured data.

1. *Slat Cove*

We start our discussion with a global inspection of the instantaneous spanwise vortical structures within the slat cove region. Figure 5 shows contours of spanwise vorticity distributions across a spanwise cut compared between experiments, 3D URANS [26,27] and the present LBM–VLES simulations at AOA of 4 deg. The primary objective of showing Fig. 5 is to elucidate the methodology of the LBM–VLES approach in capturing the most complex unsteady flow physics in a high-lift configuration. As seen from Fig. 5, the PIV measurements from the experiments indicate two states of the slat cove unsteadiness. The first state depicts an organized train of vortical structures with much of the flow entrained into the slat cove region, and second state is the ejection of vortices through the slat gap. The aforementioned two slat cove states are globally well predicted by the present study on par with the 3D URANS [26,27] simulations, as seen from Fig. 5. However, minor discrepancies between URANS and LBM–VLES simulations in terms of local flow structure are imminent here. Slat cove state 1 clearly shows a stronger instantaneous shear layer when compared to that of URANS. Such strengthening of the shear layer is obviously due to increased flow velocities near the slat cusp. Because of the relatively higher shear-layer strength in LBM–VLES computations, the evolving shear layer breaks up into discrete vortices much later than that of URANS. Consequently, the presence of high positive vorticity leads to a chaotic breakdown of vortices into much smaller ones at the reattachment point. This observation is consistent with higher averaged TKE levels observed in the reattachment region for the present simulations. Slat cove state 2 also validates the observation of stronger recirculation in the slat cove with LBM–VLES simulations. Hence, though the qualitative nature of the unsteadiness is well predicted by both URANS and LBM–VLES simulations, local flow features are quite different. This difference is mainly attributed to the quasi-laminar modeling approach used in URANS inside the slat cove compared to the fully turbulent mode simulations of LBM–VLES.

2. *Slat Trailing Edge*

Driven by the motivation to capture the slat trailing-edge unsteadiness, we next present instantaneous snapshots of spanwise vorticity distributions around the trailing-edge region. Figure 6 shows related experimental contours of vorticity depicting the three

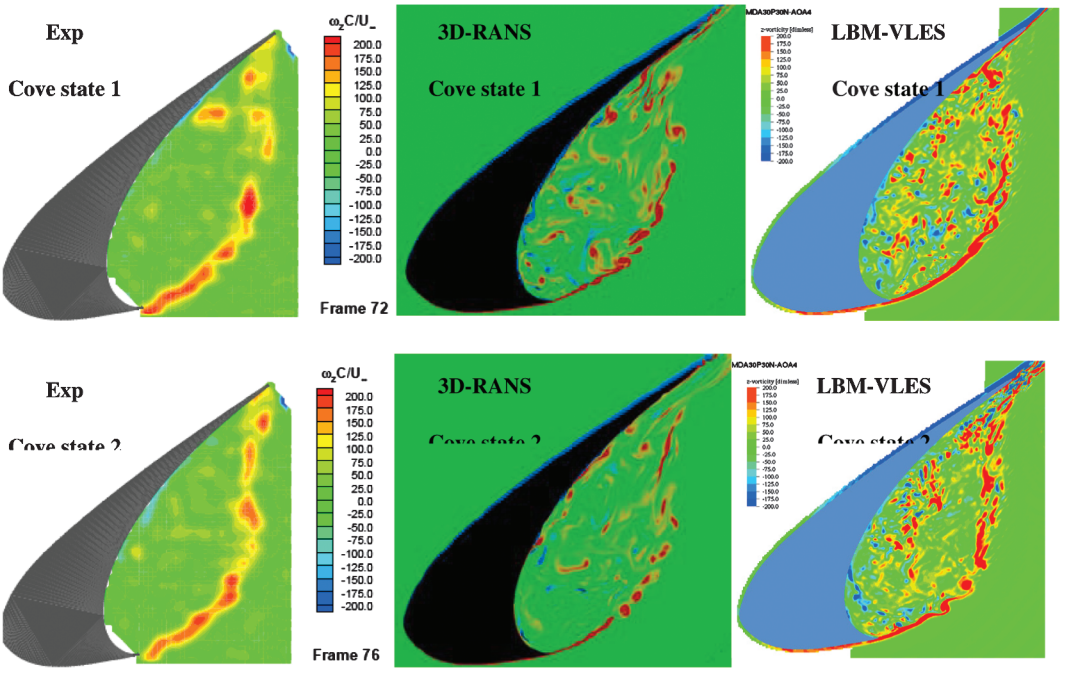

Fig. 5 Instantaneous slat cove spanwise vorticity comparisons between experiments (Jenkins et al. [21]), 3D URANS (Choudhari and Khorrami [26]), and LBM–VLES computations at AOA = 4.

different states: state 1 (two-sided shedding), state 2 (two-sided shedding and ejection through slat gap), and state 3 (one-sided shedding and ejection through slat gap). The reader is advised to refer to Choudhari et al. [11] for a detailed explanation of the aforementioned different states. Figure 6 also shows the spanwise contours of vorticity obtained from LBM–VLES computations, replicating the three states of vortex shedding observed in experiments. Contour images from numerical predictions qualitatively capture the different trailing-edge states further validating our present LBM-based approach. To summarize, the LBM–VLES approach captures not only the mean but also the complex unsteady flow physics accurately. Such advantages of this approach can be further exploited to use the unsteady simulation data for obtaining meaningful aeroacoustics predictions.

3. *Unsteady Flow Structures: Influence of Angle of Attack*

As discussed previously, similar to experiments of Jenkins et al. [21], simulations were conducted for different angles of attack (4 and 8 deg) to infer the variation of unsteady flow dynamics with angle of attack. Visual inspection of instantaneous isosurfaces often provides valuable information about the characteristics of the local flow structure. Figure 7 show isosurfaces colored by vorticity magnitude around the slat region at different angles of attack. For all of the studied angles of attack, it can be observed that a well defined shear layer near the slat cusp rapidly breaks up into smaller discrete corotating vortices containing peak vorticity levels. When the angle of attack increases, the shear-layer disintegration region moves upstream of the slat cusp. Such behavior is expected because, at higher angle of attack (e.g., AOA = 8), the real contact angles between the formed slat shear layer and the incoming freestream velocity is reduced; this actually forms a relative compact recirculation region inside slat cove. The previous observation is clearly shown in Fig. 7, where the local flow structures near the slat cusp are clearly shown. It is interesting to note that the two-dimensional vortices in the vicinity of the slat cusp rapidly dissociate and exhibit three-dimensionality further downstream. Another interesting observation that was previously reported by Jenkins et al. [21] is how the AOA influences the vortex entrainment into the cove and ejection of vortices through slat gap. At the reattachment point, entrainment and convection of vortices into the recirculation zone is more pronounced at AOA of 4 deg. As AOA is increased, due to the approach angle of the shear layer at the slat lower surface, much of the shear-layer vortices are ejected through the slat gap and few are entrained into the recirculation zone.

C. Acoustic Implications

It is well known that the region around the leading-edge slat is an active source of both broadband and tonal noise. Figure 8 shows several acoustic probe locations within the slat cove and the slat gap regions to capture both forms of noise. As indicated by Fig. 8, probes 0 and 1 envelop the slat gap region followed by probe 2 encompassing the slat trailing-edge region. Similarly, probe 3 represents the reattachment region, and the shear layer is captured by probes 4 and 5. It should also be noted that probe locations 0, 3, 4, and 5 are specified in accordance with the probe locations of Khorrami et al. [9] for comparison purposes. As a first step, the computed unsteady pressure data at the aforementioned probe locations were postprocessed to obtain the acoustic spectrum information with 15.25 Hz bandwidth, Hanning window, and 50% overlapping. Results are presented for different angles of attack as illustrated by Fig. 8. We begin our discussion with the spectral analysis obtained in the slat gap/trailing-edge regions (probes 0, 1, and 2). Acoustic spectra for these probe locations clearly show broadband noise in the slat gap region at all AOA. Such broadband noise is primarily due to the effect of the convected turbulent eddies through the slat gap, which eventually interact with the vortices shedding from the slat trailing edge. It can be observed that the spectra for probe 0 (slat gap) shows high sound levels at lower frequencies around 2 kHz compared to probe 2 (slat trailing edge), which exhibits high sound levels in the higher frequency range of 20–40 kHz. This is expected because probe 2 falls in a region where the trailing-edge vortices continually interact with the ejected slat gap vortices. Note that there is a decrease in sound levels with increasing AOA at this particular probe location.

The broadband noise nature for upstream probes 3 and 4 is slightly undermined as seen from Fig. 8. Probe 3 in the reattachment location is clearly dominated by the lower frequencies ranging between 1–2 kHz. This is somewhat consistent with the predictions of Choudhari and Khorrami [26], who reported similar low frequencies (1.5–4 kHz) in the reattachment location. The low

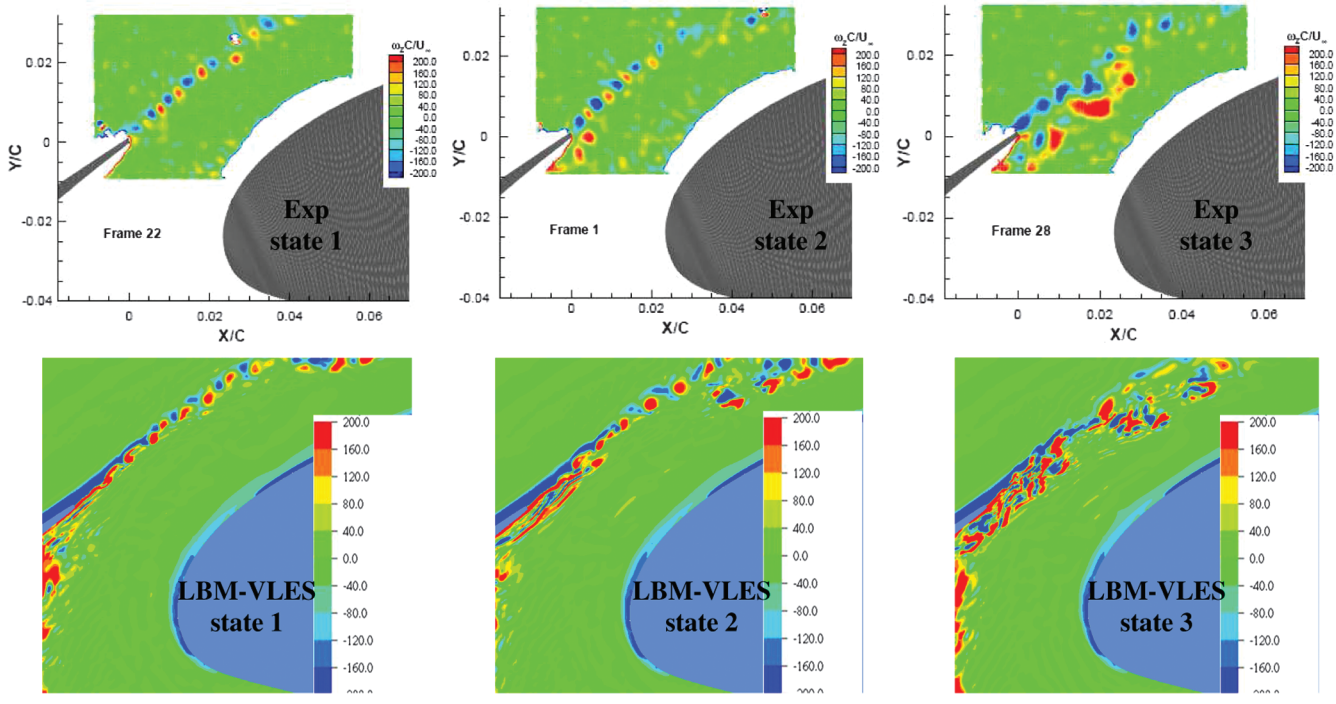

Fig. 6 Instantaneous trailing-edge spanwise vorticity comparisons between experiments (Jenkins et al. [21]) and LBM–VLES computations at AOA = 4.

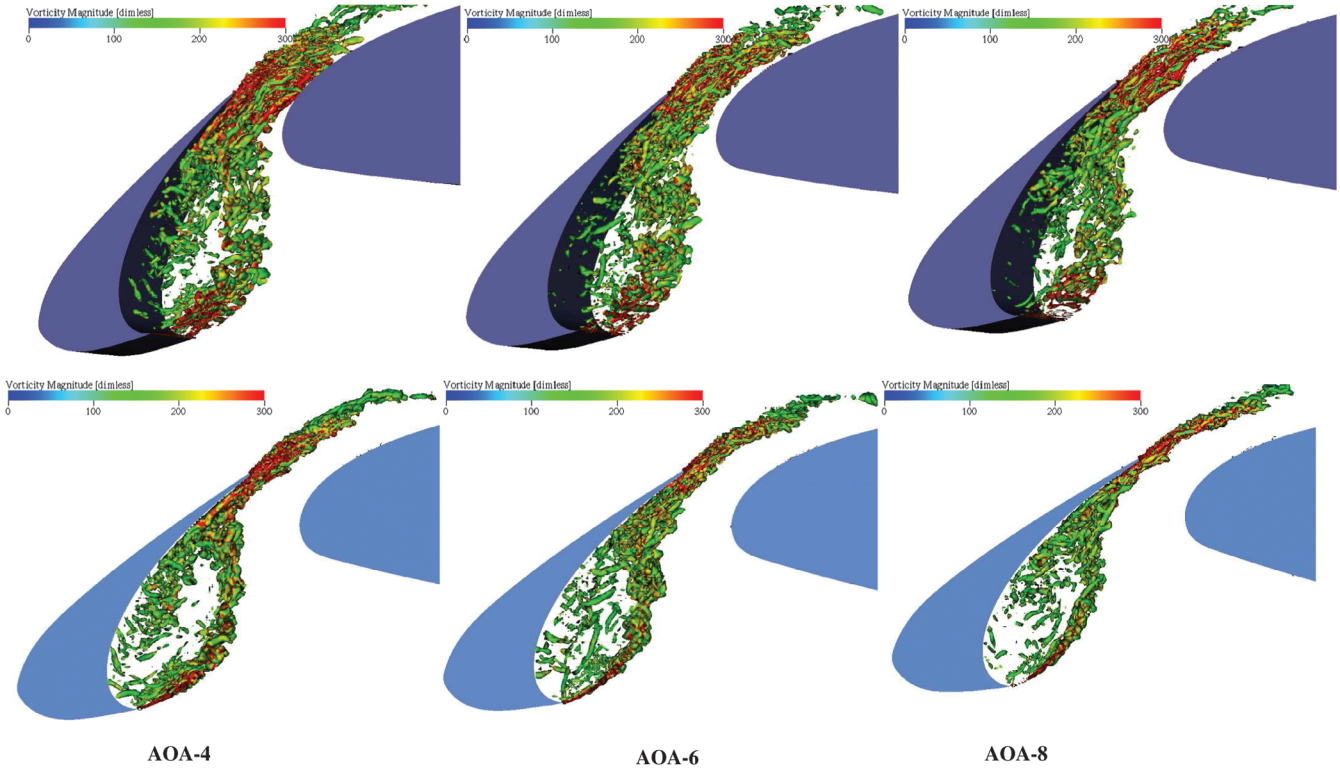

Fig. 7 Instantaneous snapshot comparisons of isosurfaces colored by vorticity magnitude for different angles of attack inside the slat cove region.

frequencies in the reattachment region are expected because the discrete vortical structures approaching the slat lower surface experience rapid distortions accompanied by flow deceleration. Similar observations are also seen for probe 4 (downstream of shear layer), whereby the thickening of the shear layer again leads to low frequencies. Further, for probe 5 the spectral plot shows a tonal peak around frequency of 10 kHz at all AOA. Such high frequency in the slat shear layer has also been reported by Khorrami et al. [9]. Similar to Khorrami et al., the spectral analysis for probes 3 to 5 illustrated that the high frequency oscillations in the free shear layer

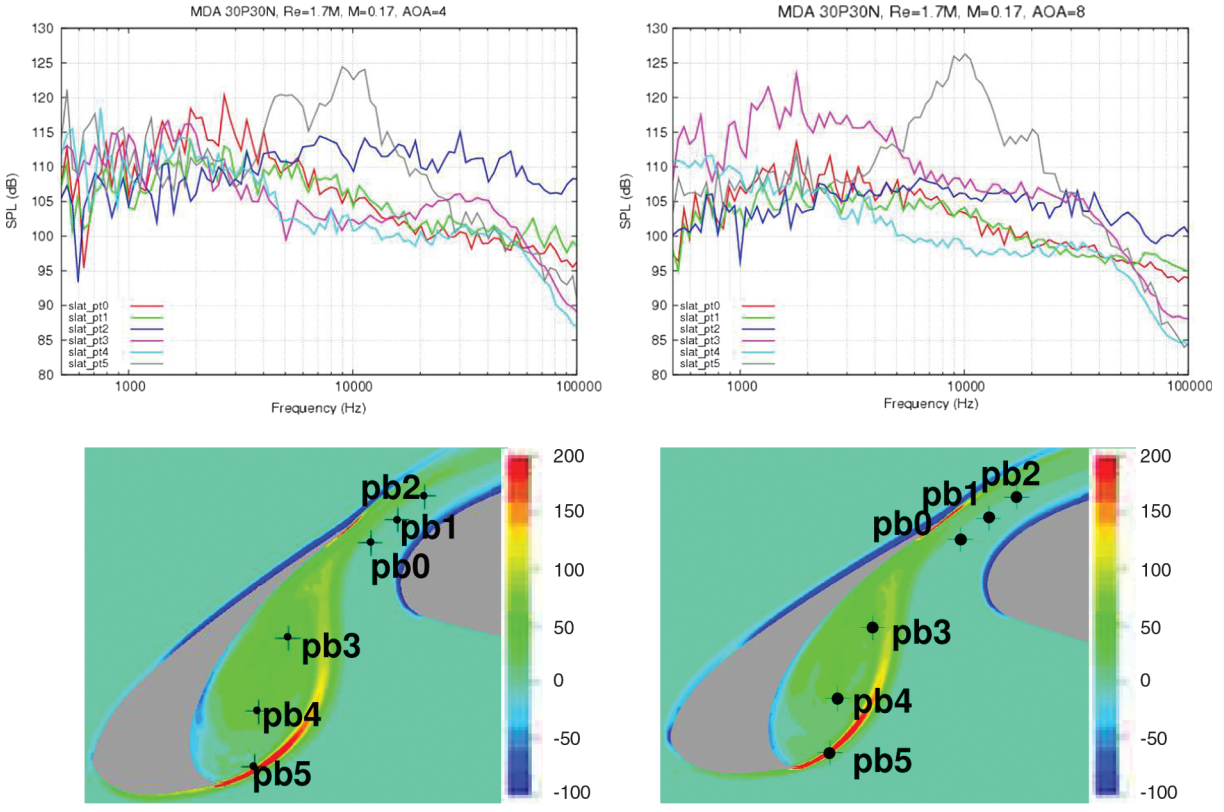

Fig. 8 Computed 1/12th-octave band SPL spectrum around the slat region at AOA = 4 (top left) and AOA = 8 (top right). At bottom, the relative locations of measurement probes on top of mean flow z vorticity contour at AOA = 4 (left) and AOA = 8 (right).

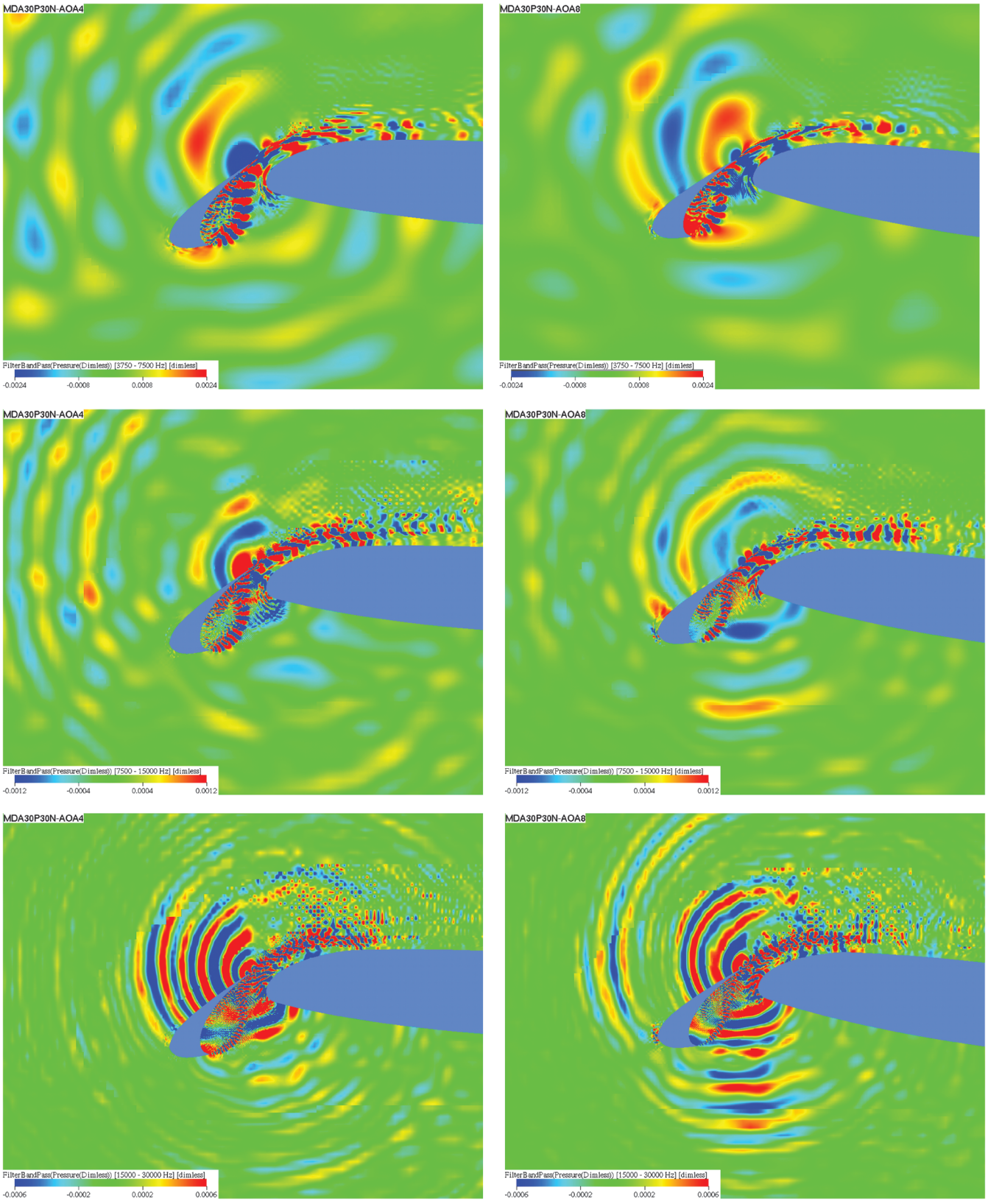

Fig. 9 Snapshot of band-filtered pressure fluctuations at different frequency bands for AOA of 4 deg (left) and 8 deg (right).

gradually dampen as the reattachment locations are reached. To summarize, the present spectral analysis based on time-accurate LBM–VLES computations provides a good qualitative representation of the slat noise sources.

Figure 9 shows snapshots of band-filtered pressure fluctuations between different frequency bands for different AOA. The blue and the red colors of the band-pass filter images indicate positive and negative pressure fluctuations. The images show the fluctuations of pressure depicting the propagation of pressure waves from the slat region. A close look at these images between different frequency bands clearly shows the directivity pattern of the radiated sound from the slat trailing edge, especially for the high-frequency band.

V. Conclusions

A lattice Boltzmann method (LBM) based turbulence-modeling approach is presented in this study and applied to simulate a multi-element airfoil typically used in commercial aircraft at low Mach number. The mean and the instantaneous flow characteristics were compared to existing experimental data as well as predictions of Navier–Stokes-based numerical studies. By modeling flow turbulence at the mesoscopic level with an extended LBM approach, time-dependent simulations were conducted to evaluate the accuracy of the present approach. The 3D simulations provided excellent mean flow predictions of surface pressures, velocity and vorticity fields around the slat region. Further, a detailed analysis of the unsteady fluid flow inside the slat cove demonstrated the capability of the present simulations in qualitatively, capturing the slat cove and slat trailing-edge states characterized by shear layer growth and breakup, trailing-edge vortex shedding and related entrainment and diffusion processes. Further, the unsteady analysis was extended to provide insight into the near-field noise radiation. Detailed flow visualization was used to provide insight into the transient nature of the flowfield inside slat cove region. This analysis identified strong pressure fluctuations being generated by the slat shear-layer vortices, flow reattachment inside the slat cove, and slat trailing-edge vortex shedding. These unsteady flow features are closely related to the near field noise radiation from the slat region.

Acknowledgments

The computations are performed with commercial computational fluid dynamics software PowerFLOW 4.0d. The authors would like to acknowledge the input from Mehdi Khorrami (NASA) for providing details on the experiments and other helpful suggestions.

References

[1] Rudolph, P. K. C., "High-Lift Systems on Commercial Subsonic Airliners," NASA CR 4746, Sept. 1996.

[2] Meredith, P., "Viscous Phenomena Affecting High-Lift Systems and Suggestions for Future CFD Development," AGARD CP 515, Sept. 1993. pp. 19-1–19-8.

[3] Hayes, J. A., Horne, W. C., Soderman, P. T., and Bent, P. H., "Airframe Noise Characteristics of a 4.7% Scale DC-10 Model," 3rd AIAA/CEAS Aeroacoustics Conference, Atlanta, GA, AIAA Paper 97-1594, May 1997.

[4] Storms, B. L., Ross, J. C., Horne, W. C., Hayes, J. A., Dougherty, R. P., Underbrink, J. R., et al., "An Aeroacoustic Study of an Unswept Wing with a Three-Dimensional High Lift System," NASA TM 112222, Feb. 1998.

[5] Dobryzynski, W., Nagakura, K., Gehlhar, B., and Buschbaum, A., "Airframe Noise Studies on Wings with Deployed High-Lift Devices," 4th AIAA/CEAS Aeroacoustics Conference, Toulouse, France, AIAA Paper 1998-2337, June 1998.

[6] Storms, B. L., Hayes, J. A., Moriarty, P. J., and Ross, J. C., "Aeroacoustic Measurements of Slat Noise on a Three-dimensional High-Lift System," 5th AIAA/CEAS Aeroacoustics Conference and Exhibit, Bellevue, WA, AIAA Paper 1999-1957, May 1999.

[7] Mendoza, F., and Brooks, T. F., "Aeroacoustics Measurements of a Wing/Slat Model," 8th AIAA/CEAS Aeroacoustics Conference and Exhibit, Breckenridge, CO, AIAA Paper 2002-2604, June 2002.

[8] Rumsey, C. L., and Ying S. X., "Prediction of High-lift: Review of Present CFD Capability," *Progress in Aerospace Sciences*, Vol. 38, No. 2, 2002, pp. 145–180. doi:10.1016/S0376-0421(02)00003-9

[9] Khorrami, M. R., Singer, B. A., and Berkmann, M. E., "Time-accurate Simulations and Acoustic Analysis of Slat Free-Shear Layer," *AIAA Journal*, Vol. 40, No. 7, July 2002, pp. 1284–1291. doi:10.2514/2.1817

[10] Khorrami, M. R., Singer, B.A., and Lockard, D. P., "Time-Accurate Simulations and Acoustic Analysis of Slat Free-Shear Layer: Part 2," 8th AIAA/CEAS Aeroacoustics Conference and Exhibit, Breckenridge, CO, AIAA Paper 2002-2579, June 2002.

[11] Choudhari, M., Khorrami, M. R., Lockard, D. P., Atkins, H., and Lilley, G., "Slat Cove Noise Modeling: A Posteriori Analysis of Unsteady RANS Simulations," 8th AIAA/CEAS Aeroacoustics Conference and Exhibit, Breckenridge, CO, AIAA Paper 2002-2468, June 2002.

[12] Khorrami, M. R., Choudhari, M., Singer, B. A., Lockard, D. P., and Streett, C. L., "In Search of the Physics: The Interplay of Experiment and Computation in Slat Aeroacoustics," 41st Aerospace Sciences Meeting and Exhibit, Reno, NV, AIAA Paper 2003-0980, Jan. 2003.

[13] Khorrami, M. R., Berkman M. E., and Choudhari, M. M., "Unsteady Flow Computations of a Slat with a Blunt Trailing Edge," *AIAA Journal*, Vol. 38, No. 11, 2000, pp. 2050–2058. doi:10.2514/2.892

[14] Singer, B. A., Lockard D. P., and Brentner, K. S., "Computational Aeroacoustic Analysis of Slat Trailing Edge Flow," *AIAA Journal*, Vol. 38, No. 9, Sept. 2000, pp. 1558–1564. doi:10.2514/2.1177

[15] McGinley, C. B., Anders, J. B., and Spaid, F. W., "Measurements of Reynolds Stress Profiles on a High-Lift Airfoil," 16th Applied Aerodynamics Conference, Albuquerque, NM, AIAA Paper 1998-2620, June 1998.

[16] Olson, S., Thomas, F. O., and Nelson, R. C., "A Preliminary Investigation into Slat Noise Production Mechanism in a High Lift Configuration," 18th AIAA Applied Aerodynamics Conference, Denver, CO, AIAA Paper 2000-4508, Aug. 2000.

[17] Olson, S., Thomas, F. O., and Nelson, R. C., "Mechanisms of Slat Noise Production in a 2D Multi-Element Airfoil Configuration," AIAA/CEAS Aeroacoustics Conference and Exhibit, Maastricht, The Netherlands, AIAA Paper 2001-2156, May 2001.

[18] Rumsey, C. L., Gatski, T. B., Ying, S. X., and Bertelrud, A., "Prediction of High-Lift Flows Using Turbulent Closure Models," *AIAA Journal*, Vol. 36, No. 5, 1998, pp. 765–774. doi:10.2514/2.435

[19] Takeda, K., Ashcroft, G. B., Zhang, X., and Nelson, P. A., "Unsteady Aerodynamics of Slat Cove Flow in a High-Lift Device Configuration," 39th Aerospace Sciences Meeting and Exhibit, Reno, NV, AIAA Paper 2001-0706, Jan. 2001.

[20] Takeda, K., and Zhang, X., "Unsteady Aerodynamics and Aeroacoustics of a High-Lift Device Configuration," 40th AIAA Aerospace Sciences Meeting and Exhibit, Reno, NV, AIAA Paper 2002-0570, Jan. 2002.

[21] Jenkins, L. N, Khorrami, M. R., and Choudhari, M. M., "Characterization of Unsteady Flow Structures Near Leading Edge Slat: Part 1. PIV Measurements," 10th AIAA/CEAS Aeroacoustics Conference , Manchester, England, U.K., AIAA Paper 2004-2801, May 2004.

[22] Deck, S., "Zonal-Detached-Eddy Simulation of the Flow Around a High-Lift Configuration," *AIAA Journal*, Vol. 43, No. 11, Nov. 2005, pp. 2372–2384. doi:10.2514/1.16810

[23] Terracol, M., Labourasse, E., Manoha, E., and Sagaut, P., "Simulation of the 3D Unsteady Flow in a Slat Cove for Noise Prediction," 9th AIAA/CEAS Aeroacoustics Conference and Exhibit, Hilton Head, SC, AIAA Paper 2003-3110, May 2003.

[24] Imamura, T., Enomoto S., Yokokawa, Y., and Yamamoto, K., "Three-Dimensional Unsteady Flow Computations Around a Conventional Slat of High-Lift Devices" *AIAA Journal*, Vol. 46, No. 5, May 2008, pp. 1045–1053. doi:10.2514/1.25660

[25] Khorrami, M. R., Choudhari, M. M., and Jenkins, L. N., "Characterization of Unsteady Flow Structures Near leading Edge Slat: Part 2. 2D Computations," 10th AIAA/CEAS Aeroacoustics Conference, Manchester, England, U.K., AIAA Paper 2004-2802, May 2004.

[26] Choudhari, M. M, and Khorrami, M. R., "Slat Cove Unsteadiness: Effect of 3D Flow Structures," 44th AIAA Aerospace Sciences Meeting and Exhibit, Reno, NV, AIAA Paper 2006-211, Jan. 2006.

[27] Choudhari, M. M., and Khorrami, M. R., "Effect of Three-Dimensional Shear-Layer Structures on Slat Cove Unsteadiness," *AIAA Journal*, Vol. 45, No. 9, 2007.

[28] Dobrzynski, W., and Pott-Pollenske, M., "Slat Noise Source Studies for Farfield Noise Prediction," AIAA/CEAS Aeroacoustics Conference and Exhibit, Maastricht, The Netherlands, AIAA Paper 2001-2158, May 2001.

[29] Chen, S., and Doolen, G., "Lattice Boltzmann Method for Fluid Flows," *Annual Review of Fluid Mechanics*, Vol. 30, 1998, pp. 329–364. doi:10.1146/annurev.fluid.30.1.329

[30] Chen, H., Chen, S., and Matthaeus, W., "Recovery of the Navier–Stokes Equations Using a Lattice-Gas Boltzmann Method," *Physical Review A*, Vol. 45, No. 8, 1992, pp. R5339–R5342. doi:10.1103/PhysRevA.45.R5339

[31] Qian, Y., d'Humieres, D., and Lallemand, P., "Lattice BGK Models for the Navier–Stokes Equation," *Europhysics Letters*, Vol. 17, 1992, pp. 479–484. doi:10.1209/0295-5075/17/6/001

[32] Li, Y., Shock, R., Zhang, R. and Chen, H., "Numerical Study of Flow Past an Impulsively Started Cylinder by Lattice Boltzmann Method," *Journal of Fluid Mechanics*, Vol. 519, 2004, pp. 273–300. doi:10.1017/S0022112004001272

[33] Li, Y., Zhang, R., Shock, R., and Chen, H., "Prediction of Vortex Shedding from a Circular Cylinder Using a Volumetric Lattice-Boltzmann Boundary Approach," *European Physical Journal Special Topics*, Vol. 171, 2009, pp. 91–97. doi:10.1140/epjst/e2009-01015-9

[34] He, X., and Luo, L., "Lattice Boltzmann Model for the Incompressible Navier–Stokes Equation," *Journal of statistical Physics*, Vol. 88, No. 3, 1997, pp. 927–944. doi:10.1023/B:JOSS.0000015179.12689.e4

[35] Chen, S., Tolke, J., Geller, S., and Krafczyk, M., "Lattice Boltzmann Model for Incompressible Axisymmetric Flows," *Physical Review E (Statistical Physics, Plasmas, Fluids, and Related Interdisciplinary Topics)*, Vol. 78, No. 4, 2008, pp. 046703. doi:10.1103/PhysRevE.78.046703

[36] Fu, S., and So, R., "Lattice Modeled Lattice Boltzmann Equation and the Constant-Density Assumption," *AIAA Journal*, Vol. 47, No. 12, 2009, pp. 3038–3042. doi:10.2514/1.41735

[37] Li, Y., Shock, R., Zhang, R., and Chen, H., "Simulation of Flow over Iced Airfoil by Using a Lattice Boltzmann Method," 43rd AIAA Aerospace Sciences Meeting and Exhibit, Reno, NV, AIAA Paper 2005-1103, Jan. 2005.

[38] Crouse, B., Senthooran, S., Balasubramanian, G., Freed, D., Noelting, S., Mongeau, L., et al., "Sunroof Buffeting of a Simplified Car Model: Simulations of the Acoustic and Flow-Induced Responses," Society of Automotive Engineers Paper 2005-01-2498, 2005.

[39] Senthooran, S., Crouse, B., Balasubramanian, G., Freed, D., and Caridi, D., "Numerical Simulation of Wind Noise on the Side Glass of a Production Automobile," International Federation of Automotive Engineering Societies Paper F2006D124, 2006.

[40] Satti, R., Li, Y., Shock, R., and Noelting, S., "Computational Aeroacoustic Analysis of a High-Lift Configuration," 46th AIAA Aerospace Sciences Meeting and Exhibit, Reno, NV, AIAA Paper 2008-34, Jan. 2008.

[41] Satti, R., Li, Y., Shock, R., and Noelting, S., "Simulation of Flow Over a 3-Element Airfoil Using a Lattice-Boltzmann Method," 46th AIAA Aerospace Sciences Meeting and Exhibit, Reno, NV, AIAA Paper 2008-549, Jan. 2008.

[42] Satti, R., Li, Y., Shock, R., and Noelting, S., "Aeroacoustics Analysis of a High-Lift Trapezoidal Wing Using a Lattice Boltzmann Method," 14th AIAA/CEAS Aeroacoustics Conference, Vancouver, AIAA Paper 2008-3048, May 2008.

[43] Satti, R., Li, Y., Shock, R., and Noelting, S., "Unsteady Flow Simulation of a High-Lift Trapezoidal Wing Using Lattice Boltzmann Method," 38th Fluid Dynamics Conference and Exhibit, Seattle, WA, AIAA Paper 2008-4145, June 2008.

[44] Li, Y., Satti, R., Lew, P., Shock, R., and Noelting, S., "Computational Aeroacoustic Analysis of Flow Around a Complex Nose Landing Gear Configuration," 14th AIAA/CEAS Aeroacoustics Conference, Vancouver, AIAA Paper 2008-2916, May 2008.

[45] Filippova, O., and Hanel, D., "Boundary-Fitting and Local Grid Refinement for Lattice–BGK Model," *International Journal of Modern Physics C*, Vol. 9, 1998, pp. 1271–1279. doi:10.1142/S012918319800114X

[46] Chen, H., Teixeira, C., and Molvig, K., "Realization of Fluid Boundary Conditions via Discrete Boltzmann Dynamics," *International Journal of Modern Physics C*, Vol. 9, 1998, pp. 1281–1292. doi:10.1142/S0129183198001151

[47] Bhatnagar, P., Gross, E., and Krook, M., "A Model for Collision Processes in Gases. 1. Small Amplitude Processes in Charged and Neutral One-Component System," *Physical Review*, Vol. 94, No. 3, 1954, pp. 511–525. doi:10.1103/PhysRev.94.511

[48] Shan, X., Yuan, X.-F., and Chen, H., "Kinetic Theory Representation of Hydrodynamics: A Way Beyond the Navier–Stokes Equation," *Journal of Fluid Mechanics*, Vol. 550, 2006, pp. 413–441. doi:10.1017/S0022112005008153

[49] Chen, H., Kandasamy, S., Orszag, S., Shock, R., Succi, S., and Yakhot, V., "Extended Boltzmann Kinetic Equation for Turbulent Flows," *Science*, Vol. 301, 2003, pp. 633–636. doi:10.1126/science.1085048

[50] Yakhot, V., and Orszag, S. A., "Renormalization Group Analysis of Turbulence. 1. Basic Theory," *Journal of Scientific Computing*, Vol. 1, No. 1, 1986, pp. 3–51. doi:10.1007/BF01061452

[51] Pervaiz, M. M., and Teixeira, C. M., "Two Equation Turbulence Modeling with the Lattice Boltzmann Method," *Proceedings of the ASME PVP Division Conference: 2nd International Symposium on Computational Technologies for Fluid/Thermal/Chemical Systems with Industrial Applications*, Boston, MA, Aug. 1999.

[52] Chen, H., Orszag, S., Staroselsky, I., and Succi, S., "Expanded Analogy Between Boltzmann Kinetic Theory of Fluid and Turbulence," *Journal of Fluid Mechanics*, Vol. 519, 2004, pp. 307–314.

[53] Fan, H., Zhang, R., and Chen, H., "Extended Volumetric Scheme for Lattice Boltzmann Models," *Physical Review E (Statistical Physics, Plasmas, Fluids, and Related Interdisciplinary Topics)*, Vol. 73, 2006, pp. 066708. doi:10.1103/PhysRevE.73.066708

[54] Ewert, R., and Emunds, R., "CAA Slat Noise Studies Applying Stochastic Sound Sources Based on Solenoidal Digital Filters," 11th AIAA/CEAS Aeroacoustics Conference, Monterey, CA, AIAA Paper 2005-2862, May 2005.

F. Ladeinde
Associate Editor